Synthesis, Characterization, and Application of Magnetic Mesoporous MCM-41-Fe_3O_4 Core-Shell Nanoparticles in the Removal of Eosin Yellow Dye

Rawaa Abd Alattar[1*], Hayder Hamied Mihsen[1], and Luma Majeed Ahmed[1,2]

[1]*Department of Chemistry, College of Science, University of Kerbala, Kerbala 56001, Iraq*

[2]*Al-Zahraa Center for Medical and Pharmaceutical Research Sciences (ZCMRS), Al-Zahraa University for Women, Karbala 56001, Iraq*

* ***Corresponding author:***

email: rawaa.a@s.uokerbala.edu.iq

Received: June 17, 2025
Accepted: November 27, 2025

DOI: 10.22146/ijc.108056

Abstract: *Spinel ferrite (Fe_3O_4) nanoparticles have been produced as a black powder using precipitation and ultrasonic methods. The framework of MCM-41 was built using sodium silicate as the source of silica and CTAB as a template. Fe_3O_4 was immobilized on MCM-41 using the microwave method at 100 °C for 20 min, yielding MCM-41-Fe_3O_4 as a brown solid powder. This characterization was performed using FTIR, XRD, BET, TGA, FESEM-EDX, VSM, AFM, and TEM. The FTIR analysis demonstrated that the MCM-41-Fe_3O_4 had been properly synthesized. Two M–O bond peaks were discovered, one for the (Fe^{3+}–O^{2-}) octahedral site and one for the (Fe^{2+}–O^{2-}) tetrahedral sites. The XRD analyses revealed that MCM-41-Fe_3O_4 was synthesized with a highly ordered hexagonal building. The particles exhibited a spherical agglomeration and appeared smooth, as observed in TEM and FESEM examinations. The EDX analysis indicates that it was formed purely from Si, Fe, and O, with a weight percentage of 100%. BET analysis indicated that the sample had a relatively high surface area. In terms of a kinetic model, it was determined that a pseudo-second-order model provided the most suitable description. The thermodynamic study revealed that physical adsorption was exothermic and the adsorption process was nonspontaneous.*

Keywords: *MCM-41-Fe_3O_4; eosin yellow dye; dye removal; adsorption kinetics; thermodynamics*

■ INTRODUCTION

Dyes are difficult to decompose due to their complex aromatic molecular structures, which confer greater stability. Given that they can be found in wastewater from various industries and that even small amounts of dyes can have toxic and detrimental effects on receiving water, dyes are considered hazardous water contaminants [1]. Eosin yellow is one example of an anionic dye [2]. Wastewater purification requires the rapid development of methods for creating inexpensive and efficient adsorbents for dye removal. Eosin yellow dye is used in this work as an adsorbent. The limited biodegradability of mono-azo groups in dyes raises worries for the environment and public health [3]. These dyes must be removed from the aqueous form right away due to their toxicity.

Different kinds of adsorbents are effective at removing dyes. Additionally, recent research indicates that rice husks are a natural source of amorphous silica [4]—a by-product of the manufacture of rice [5]. Rice husk can be used as a readily available and affordable raw material to produce silicate and silica compositions [6]. To produce silica materials suitable for various manufacturing and technological applications, rice husk can be utilized as an inexpensive and sustainable source of active silica [7]. One of the most significant inorganic nanomaterials is that of spinel nanocrystals due to their utility in electronic, optical, electrical, magnetic, and catalytic processes. The AB_2O_4 spinel structure is made up of A and B in the tetrahedral and binding sites for ternary cations, respectively. O stands for the oxygen anion's position. A common and fundamental test for

spinel materials is spinel ferrite [8]. Solid materials with pores in their structure are commonly referred to as porous materials [9-10]. Conversely, Fe_3O_4 magnetic nanoparticles (MNPs) are currently considered highly significant. Fe_3O_4 MNPs can be mixed with porous silica materials to form porous magnetic silica materials [11-12]. The expense of filtering and separating these components from aqueous solutions is minimal, as they can be easily removed and separated using a magnetic field in solid-liquid processes [13]. Due to its enormous surface area and structured mesoporous channels, mesoporous silica MCM-41 has been utilized as both a catalyst and a catalytic support [14]. The mesoporous silica material MCM-41 features a two-dimensional hexagonal array of mesopores with large pore sizes [15]. Some researchers have turned to waste materials, such as red clay, kaolin, rice husk, and coal fly ash, in an effort to make catalysts at reduced cost. Utilizing waste products lowers the cost of waste management and is a highly effective recycling technique [16].

Over the past few years, ferrite has been synthesized at the nanoscale using a range of physical and chemical methods. Co-precipitation, hydrothermal, sol-gel, pyrolysis, microwave-assisted [17], sonochemistry, microemulsions, mechanical milling, and electrochemical methods are all examples of synthetic techniques used in its fabrication [18]. The MCM-41-Fe_3O_4 core–shell was synthesized using the microwave-assisted technique. This approach is considered a green synthesis method compared to conventional techniques used for preparing similar composites. It offers an environmentally friendly route that minimizes the use of hazardous materials and organic solvents. Moreover, the synthesis process was completed within a short period of only 10 min at a temperature of 100 °C. The characterization of the produced MCM-41-Fe_3O_4 will be investigated using FTIR, XRD, BET, TGA, FESEM-EDX, XPS, and AFM. This composite was applied to remove eosin yellow dye from aqueous solutions under various parameters, including contact time, pH, adsorbent dose, and temperature. Additionally, the kinetic and thermodynamic parameters were also determined.

■ EXPERIMENTAL SECTION

Materials

In this experiment, the sodium nitrate ($NaNO_3$), sodium hydroxide (NaOH), and ferric sulfate ($FeSO_4{\cdot}7H_2O$) used were all purchased from BDH. Cetyltrimethylammonium bromide (CTAB, > 98%) was acquired from St. Louis, Missouri, USA-based Sigma-Aldrich. Absolute ethanol (Fluka, > 99%), acetone (Romal, > 99.7%), ammonia (Fluka, > 98%), and eosin yellow dye ($C_2OH_6Br_4Na_2O_5$) were purchased from BDH with the structure as shown in Fig. 1. All chemicals were used without additional purification.

Instrumentation

A Shimadzu 8400 spectrophotometer was used to record the FTIR spectrum of specimens that had been ground into KBr and then compressed into a disk in the 4000–400 cm^{-1} range, A Shimadzu X-ray diffractometer was used to get X-ray diffraction (XRD) patterns, a BET BELSORP MINI II equipment was utilized for nitrogen adsorption/desorption analysis, and an SDT Q600 V20.9 Build 20 instrument was employed for thermogravimetric analysis (TGA/DTA). Vibrating sample magnetometry (VSM) examination was performed using an MDKB instrument (Daneshpajouh, Iran). The sample was also subjected to atomic force microscopy (AFM) (NT-MDT/NTEGRA, Netherlands), energy-dispersive X-ray spectroscopy (EDX), and scanning electron microscopy (SEM) (FESEM MIRA III, TESCAN).

Procedure

Synthesis of Fe_3O_4 nanoparticles

Synthesis of Spinel Fe_3O_4 nanocrystals was performed by mixing 0.5 g of $NaNO_3$, 0.56 g of NaOH,

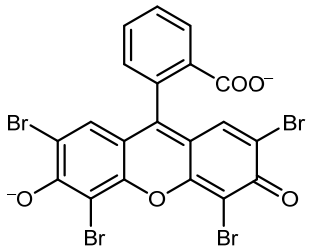

Fig 1. Structure of the eosin yellow dye

and 4 g of $FeSO_4 \cdot 7H_2O$ in 150 mL of water under ultrasonication. The final solution was then mixed using a magnetic stirrer. This murky liquid was filtered via a Buchner funnel. The residual black precipitate was dried in an oven [19].

Extraction of sodium silicate from rice husk

Initially, the rice husk was washed with deionized water to remove any grime, mud, or solid debris, and then allowed to dry. Exactly 30 g of dried rice husk was transferred to a plastic container and immersed in 500 mL of 1.0 M HNO_3 with mixing for 24 h at room temperature. After rinsing the rice husk with deionized water to ensure neutralization of the acid at a pH of 6–7, it was dried overnight at 110 °C in an oven. The rice husk was then shaken for 24 h at room temperature in 200 mL 1 M NaOH. A black filtrate (sodium silicate) [20] was obtained by filtering this mixture, which was then stored in a covered plastic container. The green method for synthesizing the sodium silicate solution from rice husk was mentioned in the reference [21].

Synthesis of MCM-41-Fe_3O_4 core–shell composite

In summary, 0.5 g of magnetic Fe_3O_4 nanoparticles was dissolved in a mixture of 120 mL of deionized water and 60 mL of ethanol. Following a half-hour ultrasonication to ensure homogeneous mixing, 1.2 mL of an aqueous ammonia solution was added, and the mixture was agitated for 1 h. To build the framework of MCM-41 in 100 mL of sodium silicate, which was utilized as the source of silica. Exactly 1 g of CTAB was added to the solution as a structure-directing agent and stirred for 1 h at room temperature. After that, the mixture was microwaved at 100 °C for 20 min and then rested for a 24-h period. The solid products were washed with ethanol and deionized water. Fermi-shell magnetosphere-containing MCM-41-Fe_3O_4 carriers were created by calcining the material for 6 h at 550 °C in air. The core-shell MCM-41-Fe_3O_4 nanocomposites created in this instance exhibited a strong magnetic response. The MCM-41-Fe_3O_4 was obtained as a brown solid powder. The steps for synthesizing MCM-41-Fe_3O_4 using the microwave method are illustrated in Fig. 2.

Removal of eosin yellow dye using MCM-41-Fe_3O_4 NPs

The adsorption of MCM-41-Fe_3O_4 was investigated by determining several adsorption kinetics parameters to assess the impact of adsorbent dose, contact time, dye concentration, temperature, and pH. A 100 mL solution of 5 g/L Eosin yellow dye and 0.05 g of the adsorbent (MCM-41-Fe_3O_4) was mixed in a glass beaker at 25 °C

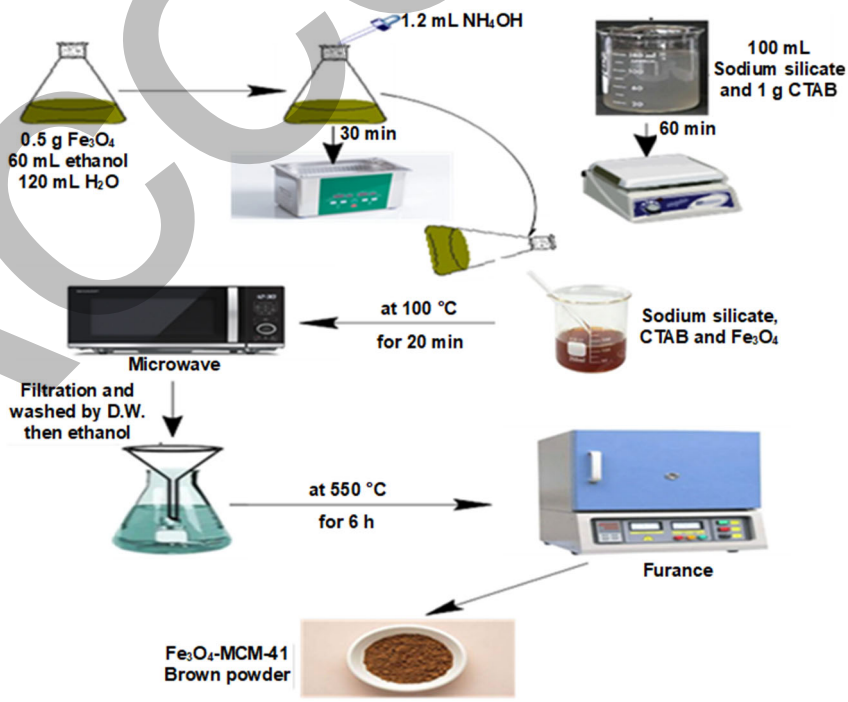

Fig 2. The steps of MCM-41-Fe_3O_4 synthesis

using magnetic stirring. Following the completion of adsorption, centrifugation (4,000 rpm) was used to separate the solution from the adsorbent at intervals of 10, 20, and 30 min. The absorbance of the solutions was measured using a UV-vis spectrophotometer at λ_{max} = 510 nm to detect the leftover dye concentration.

■ RESULTS AND DISCUSSION

FTIR Spectroscopic Analysis

To identify the organic groups on the material's surface, FTIR analysis was carried out [22], as shown in the MCM-41 findings displayed in Fig. 3(a). The silanol group (Si–OH) and the O–H groups in adsorbed water particles on the surface of the silica were identified as having a broad absorption band at about 3510 cm^{-1}. The O–H bending vibration for Si–OH groups was identified as the band at 1666 cm^{-1} [23]. The FTIR spectrum also showed bands at 825 and 1130 cm^{-1}, assigned to the symmetric and anti-symmetric stretching of Si–O–Si bonds, respectively. These findings align well with previously published research [24]. The results of MCM-41-Fe_3O_4 are shown in Fig. 3(b) as a black line. The broad absorption band at 3441 cm^{-1} is associated with adsorbed water molecules and O–H groups of Si–OH [25]. The C–H stretching vibrations are associated with the absorption band at 2928 cm^{-1} [26]. The distortion of adsorbed water molecules results in the appearance of the absorption band at 1635 cm^{-1}. The MCM-41-Fe_3O_4 was found to exhibit two distinct infrared peaks at 1091 and 802 cm^{-1}; these peaks could be attributed to the anti-symmetric and symmetric Si–O stretching vibrations [27]. The bending vibrations of the Si–O–Si lattice were apparent at 547 cm^{-1} [28]. Furthermore, in Fig. 3(c), two peaks that could be reasonably associated with the M–O bond in the nanoparticle. Absorption characteristics are located at approximately 547 and 466 cm^{-1} for the (Fe^{3+}–O^{2-}) tetrahedral site and the (Fe^{2+}–O^{2-}) octahedral site, respectively [29]. This case confirms that iron oxide (Fe_3O_4) is an inverse spinel [30], and these peaks become wider after forming the composite, as seen in Fig. 3(b).

XRD Pattern

XRD was performed to determine the essential XRD pattern of the MCM-41-Fe_3O_4, from which the broad peak

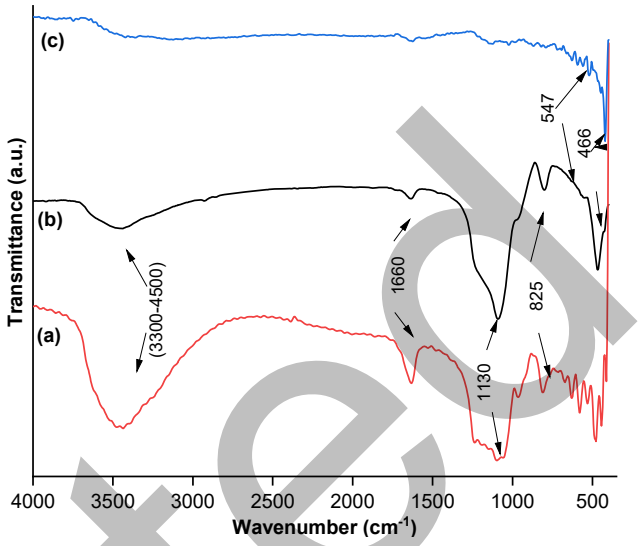

Fig 3. The FTIR spectra of (a) MCM-41, (b) MCM-41-Fe_3O_4, and (c) Fe_3O_4

in the 15–40° range is associated with amorphous silica. The peaks after it are associated with the Fe_3O_4 crystal structure [31], which thus demonstrates the presence of Fe_3O_4 in the MCM-41 structure. The XRD analysis further corroborates the findings of the FTIR analysis. The diffraction pattern exhibited well-defined peaks consistent with the crystalline structure of Fe_3O_4, matching the standard magnetite reflections (JCPDS No. 19-0629). These characteristic peaks confirm that Fe_3O_4 nanoparticles were successfully formed and embedded within the ordered mesoporous MCM-41 matrix without significantly disrupting its structural integrity. The simultaneous observation of the amorphous silica halo of MCM-41 and the sharp reflections of Fe_3O_4 in the composite pattern clearly demonstrates the coexistence of both phases. This indicates that Fe_3O_4 nanoparticles are well-dispersed within the MCM-41 channels and strongly anchored to its surface, preserving the mesoporous structure while imparting magnetic functionality to the material. The results are shown in Fig. 4. The XRD pattern of MCM-41-Fe_3O_4 and Fe_3O_4 showed diffraction lines of a high crystalline nature at 2θ angles of 11.9°, 20.1°, 24.5°, 35.8°, 62.9°, and 73.2°, which represent six diffraction peaks that correspond to the usual reflections of (220), (311), (400), (422), (440) and (511) planes, respectively [32]. The characteristic low-angle XRD pattern of MCM-41-Fe_3O_4

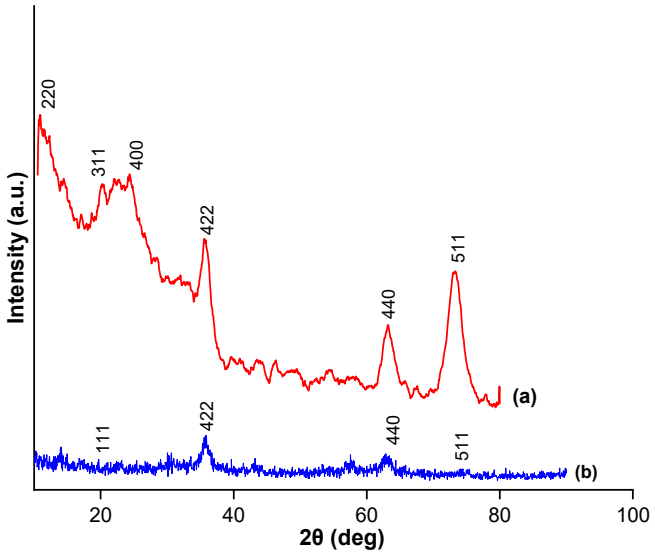

Fig 4. The high-angle XRD spectrum of (a) MCM-41-Fe_3O_4 and (b) Fe_3O_4

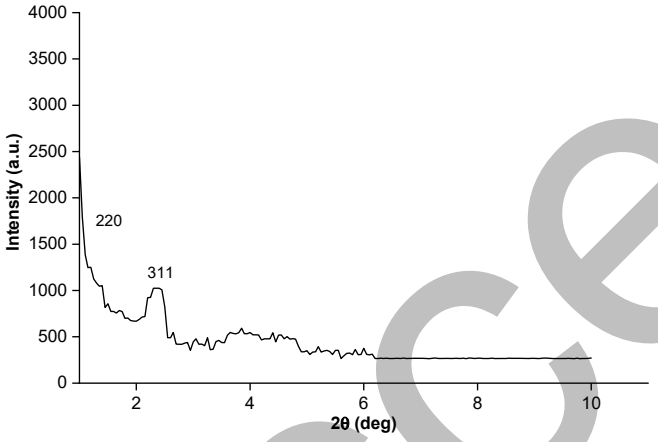

Fig 5. The low-angle XRD spectrum of MCM-41-Fe_3O_4

is illustrated in Fig. 5, which shows peaks at 2θ angles of 1.05° and 2.25° that can be attributed to the presence of a two-dimensional hexagonal mesostructure. Using low-angle XRD data and the Debye-Scherrer formula, the mean crystal size of MCM-41-Fe_3O_4 was determined to be 2.352 nm. This value refers to the composite, which is a quantum dot [33]. The crystallite size of the materials can be calculated using Eq. (1);

$$D = \frac{k\lambda}{\beta \cos\theta} \quad (1)$$

where D is the crystal size, θ is the Bragg angle, β is the full width at half maximum (FWHM) of the peak under consideration, and λ is the X-ray wavelength (1.5406 Å for Cu Kα).

Nitrogen Adsorption/Desorption Analysis

The nitrogen adsorption/desorption method was employed to investigate the specific surface area and pore size distribution of MCM-41-Fe_3O_4, with the results presented in Fig. 6(a). A type IV isotherm with a distinct H1-type hysteresis loop could be primarily responsible for the isotherm curves [34]. This indicates that MCM-41-Fe_3O_4 is mesoporous, as defined by IUPAC terminology [32]. The BET plots showed that although the porosities of MCM-41-Fe_3O_4 varied, their distribution of pore widths remained small, as is common for MCM-41 derivative materials. The pore volumes and surface areas of MCM-41-Fe_3O_4 significantly dropped compared to MCM-41. This indicates that when immobilizing Fe_3O_4

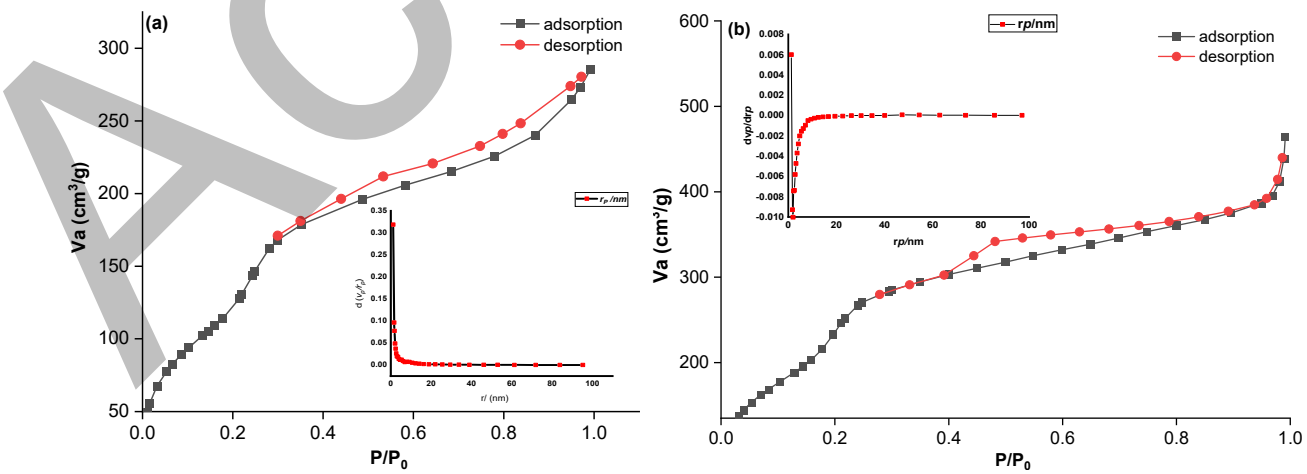

Fig 6. The nitrogen adsorption/desorption isotherm and pore size distribution of (a) MCM-41-Fe_3O_4 and (b) MCM-41

Table 1. BET analysis for MCM-41-Fe_3O_4 and starting materials

Compounds	BET surface area ($m^2\ g^{-1}$)	Total pore volume ($cm^3\ g^{-1}$)	Average pore diameter (nm)
MCM-41-Fe_3O_4	548.0	0.6999	3.2045
MCM-41	1049.2	0.7251	2.8425

onto MCM-41, the hexagonal pores at the surface are being blocked by big ligand molecules. The MCM-41-Fe_3O_4 sample had a high BET surface area of 548 m^2/g, a pore volume of 0.6999 cm^3/g, and an average pore diameter of 3.2045 nm, according to the calculation of the BET surface area and pore-size distribution. The measured surface area, average pore diameter, and pore volume for MCM-41 are 1024.9 m^2/g, 2.8425 nm, and 0.7251 cm^3/g, respectively, the results of which are shown in Fig. 6(b) and Table 1. Another indication that Fe_3O_4 forms and is incorporated into the MCM-41 framework is the decrease in the surface area of MCM-41-Fe_3O_4. It is thought that the immobilization of Fe_3O_4 in the channels of MCM-41 causes an increase in the particle size and a decrease in the surface area.

TGA/DTG Characterization

The thermal stability of MCM-41-Fe_3O_4 was examined by TGA analysis, and the results are presented in Fig. 7. The TGA study revealed a two-stage weight loss at temperatures of 131.12 and 868 °C. The DTG curve exhibits a significant peak corresponding to a weight loss of 8% during the first stage, which is a result of temperature-induced desorption of absorbed water molecules [35], whilst a weight loss of 5% during the second stage was attributed to the decomposition of MCM-41-Fe_3O_4 itself through silanol group condensation [36]. The subsequent absence of any further weight loss indicates that the support is stable up to 800 °C.

VSM Analysis

The VSM method was employed to investigate the magnetic properties of MCM-41-Fe_3O_4, with the results presented in Fig. 8(a) and 8(b). In the applied field of 9000 Oe, the saturation magnetization value of MCM-41-Fe_3O_4 was 2.8 emu g^{-1}. This is simply because the subsequent increase in Fe_3O_4 in the MCM-41-Fe_3O_4 structure led to an increase in the saturation magnetization value of

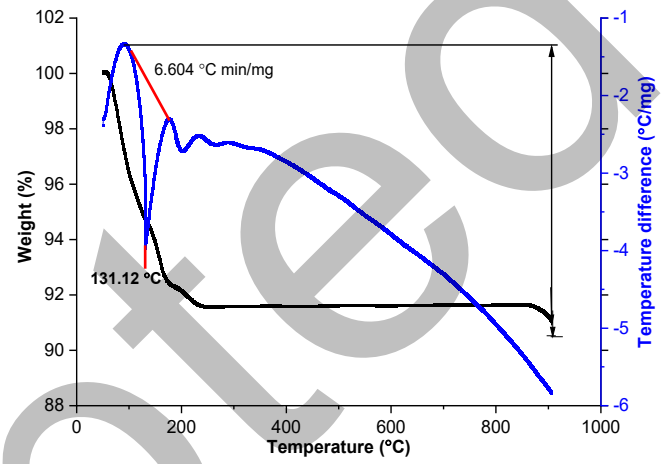

Fig 7. The TGA/DTG spectrum of MCM-41-Fe_3O_4

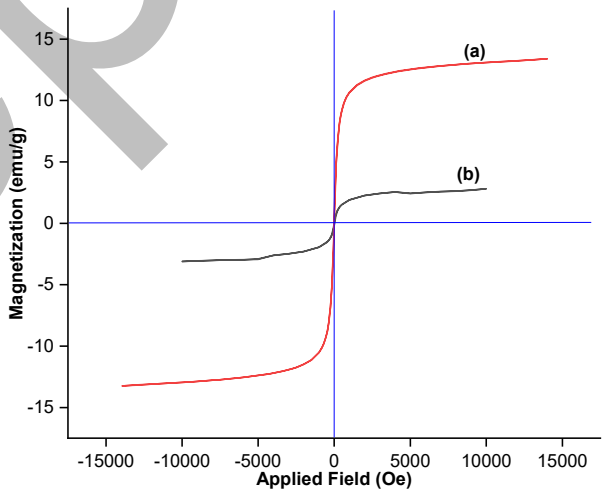

Fig 8. Magnetic properties of (a) Fe_3O_4 and (b) MCM-41-Fe_3O_4

MCM-41-Fe_3O_4. When the MCM-41 covers the Fe_3O_4 nanoparticle, the contacts between the magnetite and MCM-41 may regulate the magnetic moment's rotation, resulting in a decrease in the nanocomposite's saturation magnetization [37]. However, the incorporation of Fe_3O_4 nanoparticles into the MCM-41 matrix results in a reduction of the composite's saturation magnetization. This decrease is attributed to the lower degree of magnetization of Fe_3O_4 nanoparticles when dispersed

within the non-magnetic MCM-41 framework. Furthermore, following the MCM-41 coating and Fe_3O_4 functionalization, a further reduction in saturation magnetization was noted, which is likely due to the influence of non-magnetic surface groups surrounding the magnetic core.

FESEM and EDX of MCM-41-Fe_3O_4

The FESEM technique was carried out to investigate the particle size and morphology of the material. The SEM images of MCM-41-Fe_3O_4 are shown in Fig. 9, from which it is evident that the particles are smooth and spherical, with a particle size of 5.296 nm, confirming the shape and size of MCM-41 [38]. Based on Fig. 10, the EDX analysis of MCM-41-Fe_3O_4 indicates that the material contains silicon, oxygen, and iron. The average values for these elements (%A) were 65.89, 35.77, and 7.34%, respectively. In EDX spectroscopy, A% stands for Atomic Percent. It represents the relative number of atoms of each element present in the analyzed sample, expressed as a percentage

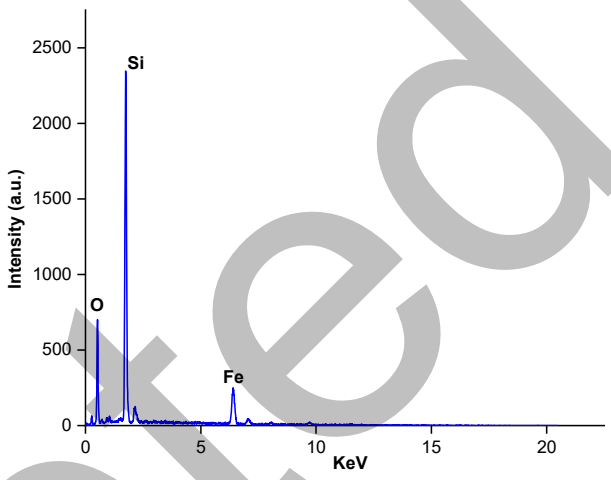

Fig 10. EDX analysis of MCM-41-Fe_3O_4

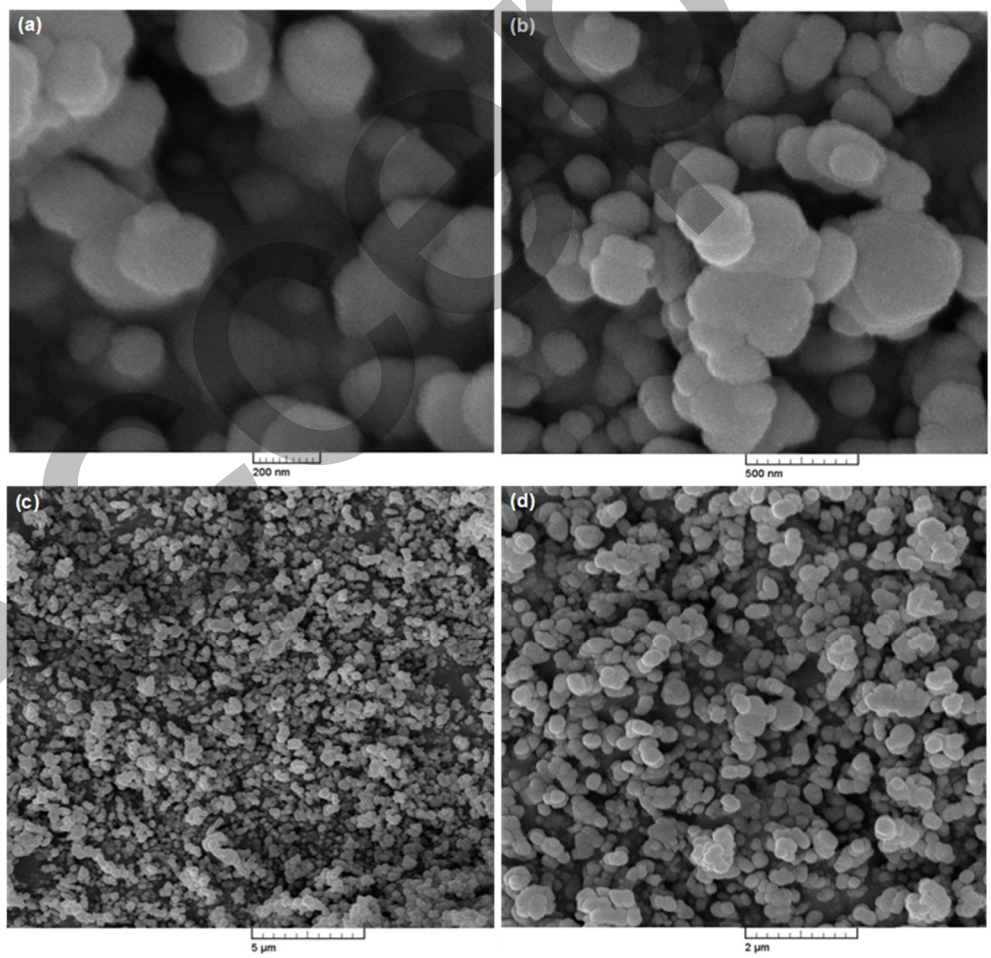

Fig 9. FESEM images of MCM-41-Fe_3O_4 at different magnifications at (a) 200 nm, (b) 500 nm, (c) 5 µm, and (d) 2 µm

of the total number of atoms detected.

AFM Analysis

The AFM technique was used to investigate the surface topography of the MCM-41-Fe_3O_4. Fig. 11 shows the AFM images and the granularity normal distribution of the MCM-41-Fe_3O_4. Moreover, AFM results indicated root mean square (RMS) and average roughness (Ra) values of 3.314 and 2.697 nm, respectively. The results showed that the average roughness of MCM-41-Fe_3O_4 was higher compared to MCM-41. This might be explained by the effective alteration of the MCM-41-Fe_3O_4 surface, which increased surface roughness and caused clusters of nanoparticles to disappear [39].

TEM Analysis

Fig. 12 shows the TEM micrographs of the immobilized magnetic core-shell nanocomposites [40]. The magnetic composite particles exhibited spherical shapes and distinct core-shell structures, which were coated with Fe_3O_4 and MCM-41 silica. In which the gray silica shell surrounds a black core of Fe_3O_4 magnetite. Additionally, their surface grew smoother than the magnetite nanoparticles'. Using the TEM images, the wall thickness and particle size were determined to be approximately 2.1 and 5.5 nm, respectively.

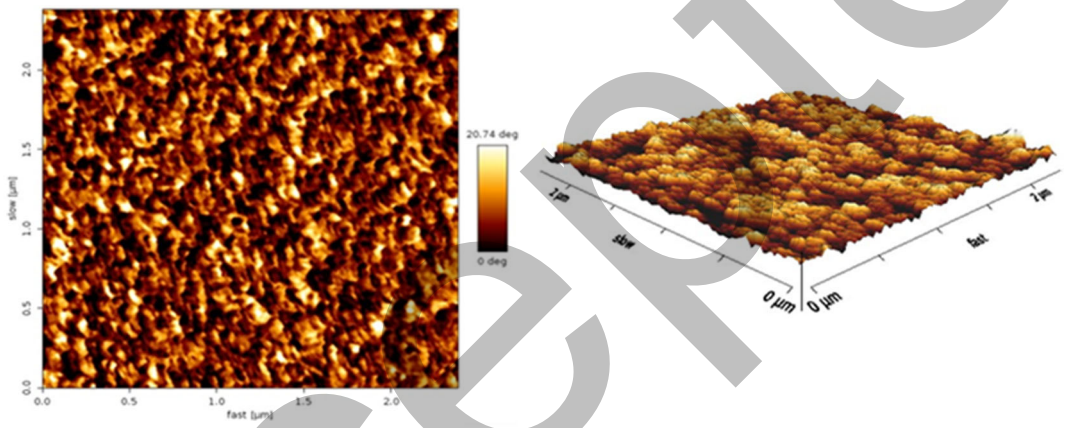

Fig 11. 2D (left) and 3D (right) AFM micrographs of MCM-41-Fe_3O_4

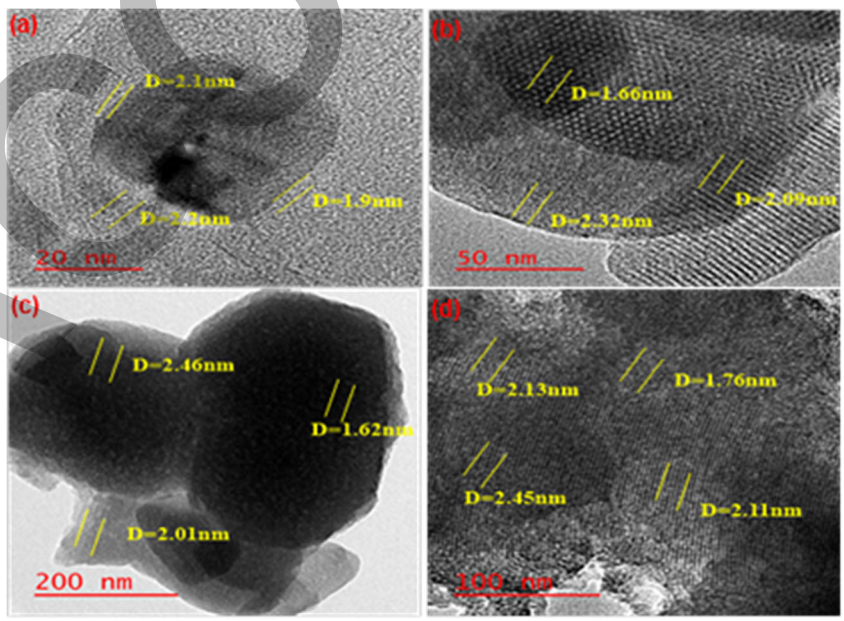

Fig 12. TEM imagery of MCM-41-Fe_3O_4 on a scale of (a) 20 nm, (b) 50 nm, (c) 200 nm, and (d) 100 nm

Removal of Eosin Yellow Dye Using MCM-41-Fe_3O_4 as an Adsorption Surface

Kinetic study

In the adsorption of eosin yellow dye using MCM-41-Fe_3O_4, several kinetic study models can be used to define the associated adsorption kinetics. Previous studies have employed pseudo-first-order and pseudo-second-order models; in this study, kinetic studies were estimated using the same models. The pseudo-first-order and pseudo-second-order kinetic models [41] can be represented as in Eq. (2) and (3), respectively;

$$\ln(q_e - q_t) = \ln q_e - k_1 t \quad (2)$$

$$\frac{t}{q_t} = \frac{1}{k_2 q_e^2} + \frac{t}{q_e} \quad (3)$$

where k_1 (min^{-1}) is the rate constant for the first-order model, k_2 (g mg^{-1} min^{-1}) is the model equilibrium rate constant for the pseudo-second-order model, and q_e and q_t (mg g^{-1}) are the quantities adsorbed at equilibrium and at an arbitrary time t (min), respectively. The results of these studies are reported in Table 2. According to the values of the correlation coefficient, R^2, the pseudo-second-order model best characterized the experimental adsorption data for the eosin yellow dye on the MCM-41-Fe_3O_4 surface. In addition, the calculated q_e values for the pseudo-second order kinetics are incredibly close to those found from the experimental data, as compared with those calculated for the pseudo-first order model. From plotting the first- and second-order reactions, as per Fig. 13(a) and 13(b) and calculating first- and second-order reaction constants for the adsorbance of Eosin yellow dye on the surface of the MCM-41-Fe_3O_4, the adsorption efficiency, %E, and the adsorption capacity at equilibrium, q_e, at a time q_t, can be measured via the use of Eq. (4–6), respectively [42]. A comparison of the adsorption capacities of different adsorbents is reported in Table 3.

$$E(\%) = \frac{C_0 - C_e}{C_0} \times 100\% \quad (4)$$

$$q_e = \frac{(C_0 - C_e) \times V}{W} \quad (5)$$

$$q_t = \frac{C_0 - C_t}{W} \times V \quad (6)$$

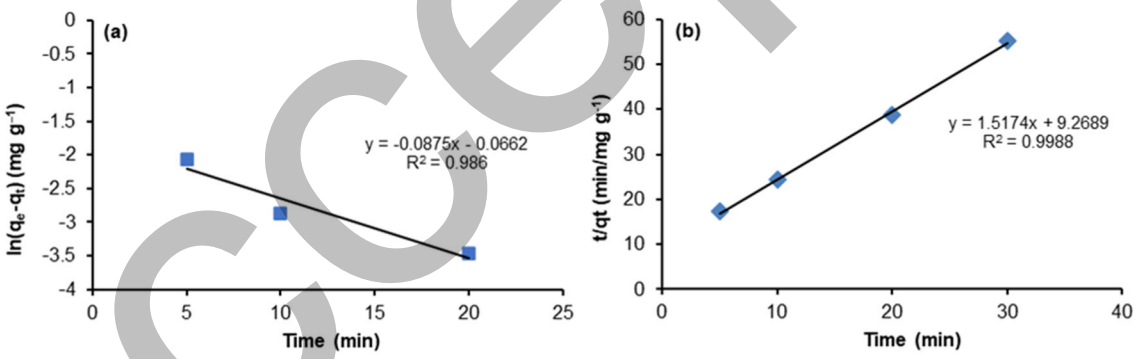

Fig 13. (a) First-order model and (b) second-order model for the adsorption of eosin yellow dye on the surface of MCM-41-Fe_3O_4

Table 2. The first- and second-order reaction parameters for eosin yellow dye on the surface of MCM-41-Fe_3O_4

Pseudo-first-order			Pseudo-second-order		
k_1 (min^{-1})	q_e (mg/g)	R^2	k_2 (g/mg.min)	q_e (mg/g)	R^2
0.0875	0.50474	0.9860	1.5174	0.6590	0.9997

Table 3. Comparison of maximum capacity, q_m (mg/g), for eosin yellow dye adsorption by various reported adsorbents

Adsorbent	Eosin yellow dye, q_{max} (mg/g)	Reference
Fe_3O_4 NPs	0.950	[43]
Fe_3O_4 with cetramide	0.431	[44]
MCM-41-Fe_3O_4	0.989	This work

The influence of MCM-41-Fe_3O_4 dose on dye removal

In the present work, to detect the optimum amount of MCM-41-Fe_3O_4, the dosage of the composite, ranging from 0.05 to 0.30 g, was mixed with 5 ppm of Eosin yellow dye at pH 8 and a stirring time of 30 min. The results, shown in Fig. 14(a) and 14(b), indicate that the percentage removal of dye increases from 60.466 to 66.320% with an increase in the dosage of the adsorbent. The adsorption constant K_{ad} and adsorption capacity also increase with the increasing dose from 0.05 to 0.3 g. These results indicate that increasing the amount of MCM-41-Fe_3O_4 led to an increase in the removal efficiencies of the dye, due to the availability of higher adsorption sites [45].

Influence of pH of the dye solution on the removal process

The effect of the pH on the adsorption of Eosin yellow dye was investigated in the range of 3–9. As indicated in Fig. 15(a) and 15(b), the removal of dye gradually increases as function of pH and the adsorption constant and adsorption capacity increase with increasing pH, the binding mechanism of anionic Eosin yellow dye on the surface of MCM-41-Fe_3O_4 is most possible to be due to electrostatic interactions between the negatively charged of dye with the positively charged surface of the MCM-41-Fe_3O_4 in the optimized pH (≈9). MCM-41-Fe_3O_4 exhibited a zero point charge at pH 7, as reported in reference [46].

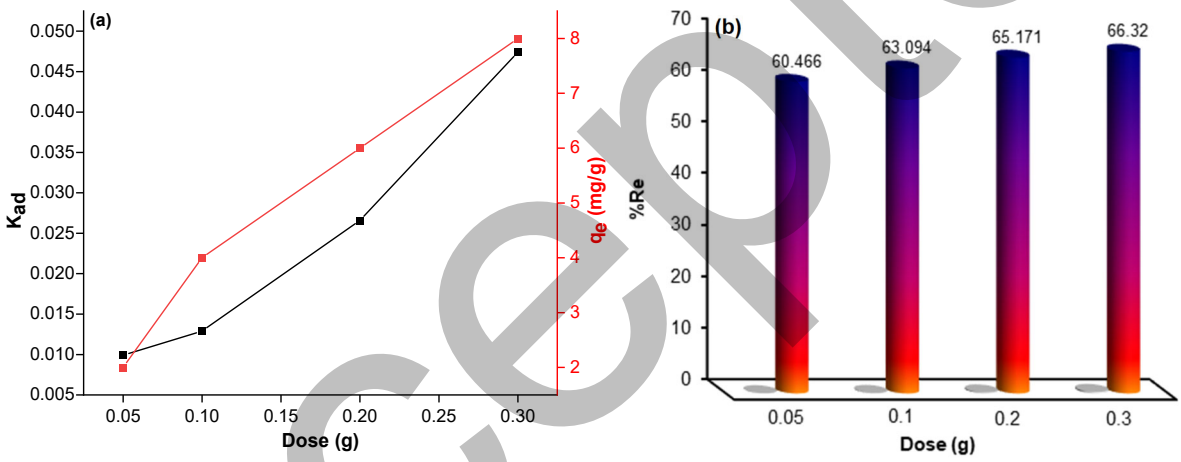

Fig 14. (a) Relationship between K_{ad} (adsorption constant), q_e (adsorption capacity), and dose. (b) Influence of MCM-41-Fe_3O_4 dose on the removal of dye

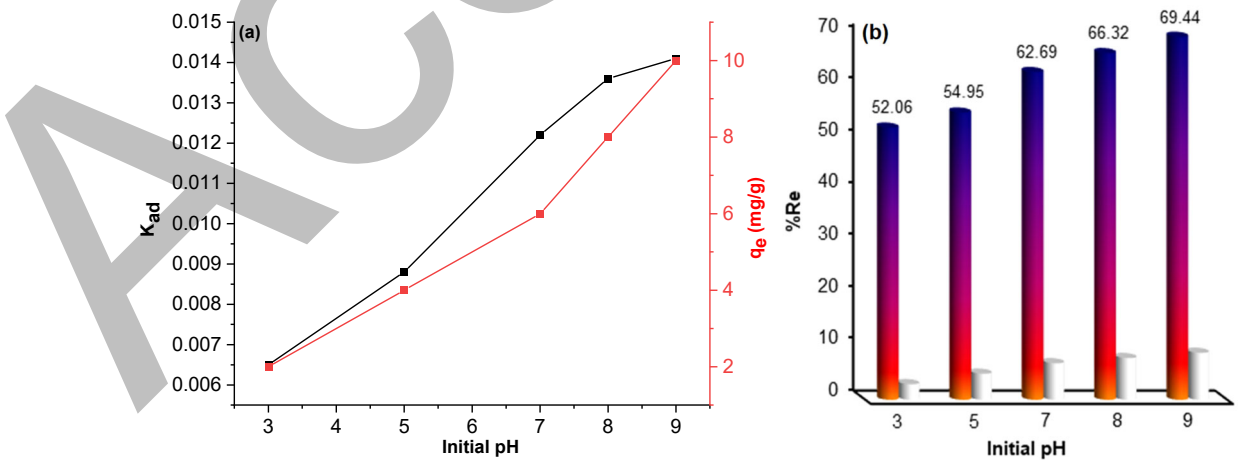

Fig 15. (a) Relationship between K_{ad} and removal efficiency versus pH, and (b) the influence of pH of the dye solution on the removal efficiency

The influence of temperature on dye removal

From the plot of the van't Hoff equation, the values of ΔH° and ΔS° can be found as the intercept and gradient of a linear fit of ln K_d versus 1000/T (Fig. 16). The interaction was found to be exothermic, with a ΔH° of −15.10064 kJ/mol. The adsorption process actually occurred on the surface of MCM-41-Fe_3O_4, as indicated by a ΔS° value of −0.02165 kJ/mol K, suggesting that the adsorbed particles were less random [47]. An exothermic reaction (negative ΔH°) occurs, indicating that the adsorption is physical (with a ΔH° value of less than 40 kJ/mol). Moreover, the ΔG° values confirm that this adsorption process is physisorption, as indicated by the values mentioned in references (−20 kJ/mol < ΔG° < 40 kJ/mol), which distinguishes it from chemisorption (−80 kJ/mol < ΔG° < −400 kJ/mol).

The Gibbs free energy can be calculated from Eq. (7). The ΔG° value was found to have positive values, indicating that the adsorption of eosin yellow dye onto MCM-41-Fe_3O_4 was nonspontaneous under experimental conditions [48]. The results of this analysis are presented in Fig. 17. The activation energy decreases when using this composite compared with its value when using MCM41. E_a is dependent on the magnitude of ΔH°, as per Eq. (8) below. That may be too low a surface area for this composite compared with the surface area value for MCM41. All associated results are reported in Table 4. Compared to many other adsorbents, MCM-41-Fe_3O_4 exhibits competitive adsorption efficiency for various pollutants, such as heavy metals and antibiotics, often exceeding the capacity of unfunctionalized MCM-41 [49]. Its kinetics are typically well-described by the pseudo-second-order model, indicating that adsorption is a chemical process. However, surface modifications and the characteristics of the pollutant influence the reaction rate. Because the reaction is exothermic, the efficiency increases with decreasing temperature. Therefore, the efficiency is found to be 75.986 at 10 °C and pH = 9, as shown in Fig. 18.

$$\Delta G^{\circ} = -RT \ln K_d \quad (7)$$

$$E_a = \Delta H^{\circ} + RT \quad (8)$$

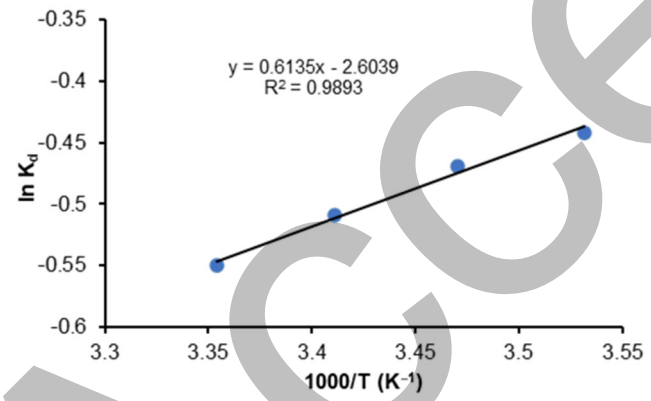

Fig 16. The van't Hoff regression of adsorption of eosin yellow dye onto MCM-41-Fe_3O_4

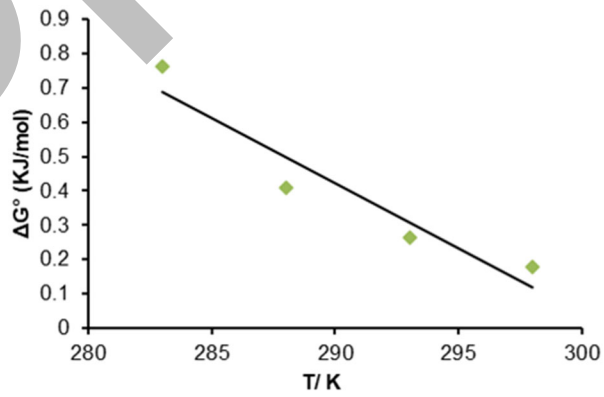

Fig 17. Relationship of ΔG° with the adsorption of eosin yellow dye versus temperature for an exothermic process

Table 4. Thermodynamic parameters determined for the adsorption of eosin yellow dye onto MCM-41-Fe_3O_4 at different temperatures

T (K)	ΔS° (kJ/mol.K)	ΔG° (kJ/mol)	ΔH° (kJ/mol)	E_a (kJ/mol)
283	−0.02165	0.76371	−15.10064	−12.67302
288	−0.02165	0.40887		−12.63145
293	−0.02165	0.265153		−12.58988
298	−0.02165	0.17953		−12.54831

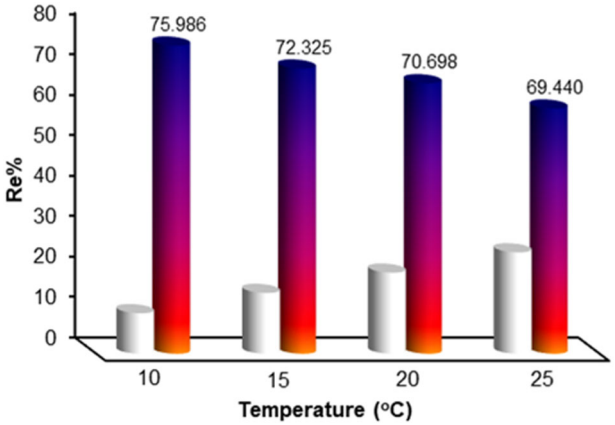

Fig 18. The efficiency relation with different temperatures of MCM-41-Fe_3O_4

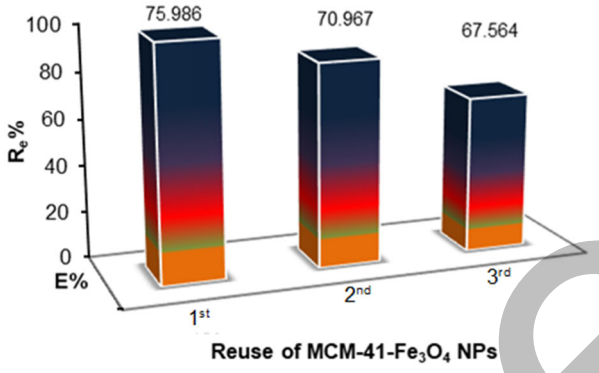

Fig 19. Reusability of MCM-41-Fe_3O_4

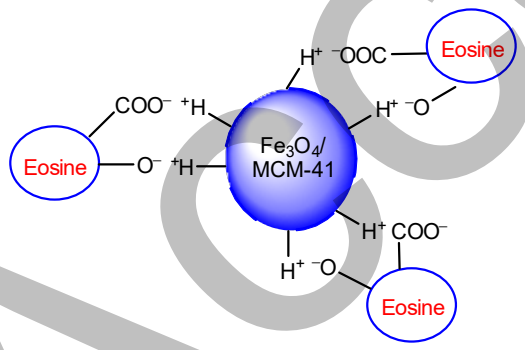

Scheme 1. The surface interactions between eosin molecules and functional groups on MCM-41-Fe_3O_4

Reusability of MCM-41-Fe_3O_4

At 0.30 g MCM-41-Fe_3O_4, 5 ppm of eosin yellow dye, at 10 °C and pH 9, the material was reused. This process was repeated three times. After that, it found that the efficiency of dye removal using MCM-41-Fe_3O_4 is 75.986%. When reused, the MCM-41-Fe_3O_4, the values decrease to 70.967 and 67.564 for the second and 3rd times, as shown in Fig. 19. In fact, the efficiency of dye removal using MCM-41-Fe_3O_4 is less than that of MCM-41 before incorporating Fe_3O_4 as a nanocomposite, which depresses the surface area and active site of MCM-41.

Mechanism of dye binding on the composite

The suggested binding mechanism of anionic eosin yellow dye on the surface of MCM-41-Fe_3O_4 is most likely due to electrostatic interactions between the negatively charged groups of the dye (–COO^- and –O^-) with the positively charged surface of the MCM-41-Fe_3O_4 in an acidic medium [24]. The adsorption mechanism, illustrating the surface interactions between Eosin molecules and functional groups on MCM-41-Fe_3O_4, is shown in Scheme 1.

■ CONCLUSION

The Fe_3O_4 nanoparticle was prepared using the precipitation method, assisted by the ultrasonic method. The incorporation of Fe_3O_4 with MCM-41 as a nanocomposite was achieved using the microwave method at 100 °C for 20 min. Through FTIR analysis, XRD, and FESEM-EDX, the presence of these nanoparticles was confirmed. The results demonstrated that MCM-41-Fe_3O_4 had a highly ordered hexagonal structure, with specific surface areas, average pore diameters, and total pore volumes of 548 $m^2 g^{-1}$, 3.2045 nm, and 0.4397 $cm^3 g^{-1}$, respectively. Also, the MCM-41-Fe_3O_4 particles were found to be spherical in shape and size. It was possible to conclude that dye adsorption increased with increasing solution temperature, contact duration, dose, and initial pH, based on the analysis of the MCM-41-Fe_3O_4 adsorbent used to remove eosin yellow dye from aqueous solutions. Our studies on the adsorption of eosin yellow dye using MCM-41-Fe_3O_4 showed that the optimal parameters were a temperature of 10 °C, an adsorption equilibrium period of 30 min, a pH of 9, a concentration of 5 ppm, and an adsorbent amount of 0.2 g. The removal of eosin yellow dye by MCM-41-Fe_3O_4 followed a pseudo-second-order kinetic model. In terms of adsorption thermodynamics, ΔH°, ΔS°, and ΔG° were calculated for MCM-41-Fe_3O_4. According to these values, the adsorption process occurs non-spontaneously, is

exothermic, and is a physical process. Therefore, MCM-41-Fe_3O_4 can be utilized as an efficient and low-cost adsorbent for the removal of dyes in industrial processes. In the future, the catalyst can be used to remove contaminated dyes and ions from wastewater.

■ ACKNOWLEDGMENTS

The authors would like to thank the University of Karbala, College of Science, Department of Chemistry, for their support in this study, particularly for the practical part, which was undertaken in their chemistry laboratory.

■ CONFLICT OF INTEREST

The authors declare no conflicts of interest concerning the publication of this paper.

■ AUTHOR CONTRIBUTIONS

Rawaa Abd Alattar performed the whole experiment and contributed to writing the manuscript. Hayder Hamied Mihsen supervised the study, conceived the ideas, interpreted the physical characterization, and wrote the manuscript. Luma Majeed Ahmed co-supervised the study and explained the effects of the prepared compounds on the removal of eosin yellow by MCM-41-Fe_3O_4 material. All authors have approved the final version of the manuscript.

■ REFERENCES

[1] Mousavi, S.R., Asghari, M., and Mahmoodi, N.M., 2020, Chitosan-wrapped multiwalled carbon nanotube as filler within PEBA thin film nanocomposite (TFN) membrane to improve dye removal, *Carbohydr. Polym.*, 237, 116128.

[2] Wen, Z., Gao, D., Niu, H., Lin, J., Li, Z., Zeng, J., Ke, F., Zhang, F., Xia, Z., and Wang, D., 2023, Three-dimensional porous adsorbent based on chitosan-alginate-cellulose sponge for selective and efficient removal of anionic dyes, *J. Environ. Chem. Eng.*, 11 (5), 110831.

[3] Shah, S.S., Sharma, T., Dar, B.A., and Bamezai, R.K., 2021, Adsorptive removal of methyl orange dye from aqueous solution using populous leaves: Insights from kinetics, thermodynamics and computational studies, *Environ. Chem. Ecotoxicol.*, 3, 172–181.

[4] Chun, J., Mo Gu, Y., Hwang, J., Oh, K.K., and Lee, J.H., 2020, Synthesis of ordered mesoporous silica with various pore structures using high-purity silica extracted from rice husk, *J. Ind. Eng. Chem.*, 81, 135–143.

[5] Hello, K.M., Mihsen, H.H., and Mosa, M.J., 2014, Modification of silica with 2,4-dinitrophenylhydrazanomethylphenol for monosaccharide productions, *Iran. J. Catal.*, 4 (3), 195.

[6] Hossain, S.S., and Roy, P.K., 2020, Waste rice husk ash derived sol: A potential binder in high alumina refractory castables as a replacement of hydraulic binder, *J. Alloys Compd.*, 817, 152806.

[7] Hossain, S.S., Yadav, S., Majumdar, S., Krishnamurthy, S., Pyare, R., and Roy, P.K., 2020, A comparative study of physico-mechanical, bioactivity and hemolysis properties of pseudo-wollastonite and wollastonite glass-ceramic synthesized from solid wastes, *Ceram. Int.*, 46 (1), 833–843.

[8] Kadhem, F.H., Ahmed, L.M., Abed, S.A., Tami, A.N., and Wan Salleh, W.M.N.H., 2025, Friendly green synthesis of cerium oxide nanoparticles using *Citrus aurantuim* extract and applied in removal of eosin yellow dye, *J. Nanostruct.*, 15 (4), 2553–2571.

[9] Hossain, S.S., Mathur, L., Bhardwaj, A., and Roy, P.K., 2019, A facile route for the preparation of silica foams using rice husk ash, *Int. J. Appl. Ceram. Technol.*, 16 (3), 1069–1077.

[10] Ghorbani, F., Kamari, S., Zamani, S., Akbari, S., and Salehi, M., 2020, Optimization and modeling of aqueous Cr(VI) adsorption onto activated carbon prepared from sugar beet bagasse agricultural waste by application of response surface methodology, *Surf. Interfaces*, 18, 100444.

[11] Sanati, A.M., Kamari, S., and Ghorbani, F., 2019, Application of response surface methodology for optimization of cadmium adsorption from aqueous solutions by Fe_3O_4@SiO_2@APTMS core–shell magnetic nanohybrid, *Surf. Interfaces*, 17, 100374.

[12] Mirheidari, M., and Safaei-Ghomi, J., 2021, Design, synthesis, and catalytic evaluation of aluminum-incorporated magnetic core–shell mesoporous

microsphere catalyst $NiFe_2O_4$@SiO_2@Al-MS for the synthesis of functionalized indenopyrazolones, *Appl. Organomet. Chem.*, 35 (8), e6274.

[13] Ghorbani, F., and Kamari, S., 2019, Core–shell magnetic nanocomposite of Fe_3O_4@SiO_2@NH_2 as an efficient and highly recyclable adsorbent of methyl red dye from aqueous environments, *Environ. Technol. Innovation*, *14*, 100333.

[14] Ramazani, Z., Elhamifar, D., Norouzi, M., and Mirbagheri, R., 2019, Magnetic mesoporous MCM-41 supported boric acid: A novel, efficient and ecofriendly nanocomposite, *Composites, Part B*, 164, 10–17.

[15] Hatem, R.S., Hussain, A.F., and Mihsen, H.H., 2024, Green synthesis, characterization, and adsorption of Co(II) and Cu(II) ions from aqueous solution by mesoporous silica MCM-41, *Chem. Pap.*, 78 (11), 6331–6342.

[16] Hülsey, M.J., Yang, H., and Yan, N., 2018, Sustainable routes for the synthesis of renewable heteroatom-containing chemicals, *ACS Sustainable Chem. Eng.*, 6 (5), 5694–5707.

[17] Alattar, R.A., 2025, Microwave-assisted green synthesis of SBA-15 and its application on photodecolorization of eosin yellow dye, *Al-Zahraa J. Health Med. Sci.*, 3 (2), 91–104.

[18] Hameed, M.A., and Ahmed, L.M., 2024, Controllable cetrimide – assisted hydrothermal synthesis of $MoFe_2O_4$ and coupling with Al_2O_3 as an effective photocatalyst for decolorization of indigo carmine dye, *Indones. J. Chem.*, 24 (1), 170–184.

[19] Mohammad, H.M., Saeed, S.I., and Ahmed, L.M., 2023, Ease Synthesis of broccoli-like Fe_3O_4 Nanostructures for superior removal of eosin yellow dye, *J. Nanostruct.*, 13 (2), 483–494.

[20] Mihsen, H.H., and Sobh, H.S., 2018, Preparation and characterization of thiourea-silica hybrid as heterogeneous catalyst, *Asian J. Chem.*, 30 (5), 937–943.

[21] Ali, H.H., Hussein, K.A., and Mihsen, H.H., 2023, Antimicrobial applications of nanosilica derived from rice grain husks, *Silicon*, 15 (13), 5735–5745.

[22] Attol, D.H., Mihsen, H.H., Jaber, S.A., Alwazni, W.S., and Eesa, M.T., 2023, Synthesis of organic functionalized silica from rice husk as an antibacterial agents, *Silicon*, 15 (5), 2349–2357.

[23] Mihsen, H.H., Rfaish, S.Y., Abass, S.K., and Sobh, H.S., 2018, Synthesis and characterization of silica-thioamide hybrid compounds derived from rice husk ash with expected biological and catalytic activity, *J. Global Pharma Technol.*, 10 (11), 590–598.

[24] Suyanta, S., and Kuncaka, A., 2011, Utilization of rice husk as raw material in synthesis of mesoporous silicates MCM-41, *Indones. J. Chem.*, 11 (3), 279–284.

[25] Timofeeva, M.N., Kalashnikova, G.O., Shefer, K.I., Mel'gunova, E.A., Panchenko, V.N., Nikolaev, A.I., and Gil, A., 2020, Effect of the acid activation on a layered titanosilicate AM-4: The fine-tuning of structural and physicochemical properties, *Appl. Clay Sci.*, 186, 105445.

[26] Radica, F., Mura, S., Carboni, D., Malfatti, L., Garroni, S., Enzo, S., Della Ventura, G., Tranfo, G., Marcelli, A., and Innocenzi, P., 2020, Phenyl-modified hybrid organic-inorganic microporous films as high efficient platforms for styrene sensing, *Microporous Mesoporous Mater.*, 294, 109877.

[27] Xie, W., and Zang, X., 2016, Immobilized lipase on core–shell structured Fe_3O_4–MCM-41 nanocomposites as a magnetically recyclable biocatalyst for interesterification of soybean oil and lard, *Food Chem.*, 194, 1283–1292.

[28] Molaei, S., and Ghadermazi, M., 2020, Selective and efficient oxidation of sulfides and thiols to their corresponding sulfoxides and disulfides catalyzed with praseodymium (III) and dysprosium (III) isonicotinamide (INA) complexes grafted onto modified mesoporous MCM-41, *Solid State Sci.*, 100, 106091.

[29] Baabu, P.R.S., Kumar, H.K., Gumpu, M.B., Babu K.J., Kulandaisamy, A.J., and Rayappan, J.B.B., 2022, Iron oxide nanoparticles: A review on the province of its compounds, properties and biological applications, *Materials*, 16 (1), 59.

[30] Zhang, J., Shang, X., Ren, H., Chi, J., Fu, H., Dong, B., Liu, C., and Chai, Y., 2019, Modulation of

inverse spinel Fe_3O_4 by phosphorus doping as an industrially promising electrocatalyst for hydrogen evolution, *Adv. Mater.*, 31 (52), 1905107.

[31] Chai, P.V., Mahmoudi, E., Teow, Y.H., and Mohammad, A.W., 2017, Preparation of novel polysulfone-Fe_3O_4/GO mixed-matrix membrane for humic acid rejection, *J. Water Process Eng.*, 15, 83–88.

[32] Abdollahi-Alibeik, M., and Ramazani, Z., 2022, Synthesis, characterization and application of magnetic mesoporous Fe_3O_4@Fe-Cu/MCM-41 as efficient and recyclable nanocatalyst for the Buchwald-Hartwig C-N cross-coupling reaction, *J. Chem. Sci.*, 134 (3), 77.

[33] Al Rihaymee, L.M.A., 2013, Enhanced Photocatalytic Activity of Titanium Dioxide Nanoparticles by Metal Deposition, *Dissertation*, University of Babylon-College of Science, Iraq.

[34] Abbas, S.K., Hassan, Z.M., Mihsen, H.H., Eesa, M.T., and Attol, D.H., 2020, Uptake of nickel(II) ion by silica-*o*-phenylenediamine derived from rice husk ash, *Silicon*, 12 (5), 1103–1110.

[35] Galacho, C., Carrott, M.M.L.R., and Carrott, P.J.M., 2008, Evaluation of the thermal and mechanical stability of Si-MCM-41 and Ti-MCM-41 synthesised at room temperature, *Microporous Mesoporous Mater.*, 108 (1-3), 283–293.

[36] Vaysipour, S., Rafiee, Z., and Nasr-Esfahani, M., 2020, Synthesis and characterization of copper (II)-poly(acrylic acid)/M-MCM-41 nanocomposite as a novel mesoporous solid acid catalyst for the one-pot synthesis of polyhydroquinoline derivatives, *Polyhedron*, 176, 114294.

[37] Kamari, S., and Ghorbani, F., 2021, Extraction of highly pure silica from rice husk as an agricultural by-product and its application in the production of magnetic mesoporous silica MCM–41, *Biomass Convers. Biorefin.*, 11 (6), 3001–3009.

[38] Si, Z., Wang, Z., Cai, D., Li, G., Li, S., and Qin, P., 2020, A high-permeance organic solvent nanofiltration membrane via covalently bonding mesoporous MCM-41 with polyimide, *Sep. Purif. Technol.*, 241, 116545.

[39] Lam, C.D., and Park, S., 2025, Nanomechanical characterization of soft nanomaterial using atomic force microscopy, *Mater. Today Bio*, 31, 101506.

[40] Qiao, J., Gao, Y., Zheng, K., Shen, C., Jia, A., and Zhang, Q., 2025, One-pot synthesis of magnetic core-shell Fe_3O_4@C nanospheres with Pt nanoparticle immobilization for catalytic hydrogenation of nitroarenes, *Appl. Sci.*, 15 (10), 5773.

[41] Mukhlis, M., Hidayah, N., Hanifah, A., Itnawira, I., Anita, S., Devi, S., and Tamboesai, E.M., 2025, Optimization of contact time and stirring speed in the adsorption of Cd(II) using *Acacia crassicarpa* bark powder as adsorbent, *Indones. J. Chem. Anal.*, 8 (2), 111–120.

[42] Chen, S., Qin, C., Wang, T., Chen, F., Li, X., Hou, H., and Zhou, M., 2019, Study on the adsorption of dyestuffs with different properties by sludge-rice husk biochar: adsorption capacity, isotherm, kinetic, thermodynamics and mechanism, *J. Mol. Liq.*, 285, 62–74.

[43] Bibi, S., Ahmad, A., Shah, S.S., Siddiq, M., Habila, M.A., and Choi, D., 2024, Synthesis of Cit-Fe_3O_4@TiO_2 photocatalyst for the degradation of eosin-Y and methylene blue dye, *Ceram. Int.*, 50 (20, Pt. A), 37533–37540.

[44] Hassan, A.A., Ali, M.E.M., Abdel-Latif, S.A., Hasani, I.W., and Fahim, Y.A., 2025, Efficient removal of Remazol Red dye from aqueous solution using magnetic nickel ferrite nanoparticles synthesized via aqueous reflux, *Sci. Rep.*, 15 (1), 17527.

[45] Fakhri, F.H., and Ahmed, L.M., 2019, Incorporation CdS with ZnS as composite and using in photo-decolorization of Congo red dye, *Indones. J. Chem.*, 19 (4), 936–943.

[46] Ulu, A., Noma, S.A.A., Koytepe, S., and Ates, B., 2018, Magnetic Fe3O4@MCM-41 core–shell nanoparticles functionalized with thiol silane for efficient l-asparaginase immobilization, *Artif. Cells, Nanomed., Biotechnol.*, 46 (sup2), 1035–1045.

[47] Iryani, A., Nur, H., Santoso, M., and Hartanto, D., 2020, Adsorption study of rhodamine B and methylene blue dyes with ZSM-5 directly

synthesized from Bangka kaolin without organic template, *Indones. J. Chem.*, 20 (1), 130–140.

[48] Lafi, R., Mabrouk, W., Al Zahrani, A.Y.A., Hafiane, A., Keshk, S.M.A.S., and Montasser, I., 2024, Methyl orange adsorption onto modified extracted cellulose from olive stones: Kinetics, isotherms, thermodynamic, mechanism studies, and desorption, *Water Conserv. Sci. Eng.*, 9 (2), 38.

[49] Guo, Y., Chen, B., Zhao, Y., and Yang, T., 2021, Fabrication of the magnetic mesoporous silica Fe-MCM-41-A as efficient adsorbent: Performance, kinetics and mechanism, *Sci. Rep.*, 11 (1), 2612.